A Numerical Study of the Diurnal Cycle of Tropical Oceanic Convection

CHANGHAI LIU AND MITCHELL W. MONCRIEFF

National Center for Atmospheric Research, Boulder, Colorado*

(Manuscript received 2 December 1996, in final form 28 October 1997)

ABSTRACT

Idealized two-dimensional cloud-resolving numerical modeling was conducted to investigate the diurnal variability of deep tropical oceanic convection. The model was initialized with a horizontally homogeneous atmosphere upon which a uniform and time-independent large-scale forcing was imposed. The underlying surface was assumed to be an open ocean with a constant sea surface temperature. Emphasis was on two distinct regimes: (a) highly organized squall-line-like convection in strong ambient shear and (b) less organized nonsquall cloud clusters without ambient shear.

A pronounced diurnal cycle was simulated for the highly organized case; convective activity and intensity attained a maximum around predawn and a minimum in the late afternoon. A similar diurnal variability was obtained for the less organized case and was characterized by more precipitation during the night and early morning and less precipitation in the afternoon and evening.

The modeled diurnal variation was primarily attributed to the direct interaction between radiation and convection, whereas the cloud–cloud-free differential heating mechanism played a secondary role.

When the radiative effect of clouds was excluded, a diurnal cycle was still present. Moreover, the cloud radiative forcing had a negative influence on precipitation/convective activity, in contrast with general circulation modeling results.

1. Introduction

The diurnal variation of deep precipitating convection is a well-known phenomenon in both Tropics and midlatitudes and has been extensively studied from surface rainfall observations (e.g., Wallace 1975; Gray and Jacobson 1977; McGarry and Reed 1978; Janowiak et al. 1994), and from the satellite or radar-derived cloudiness and precipitation (e.g., Reed and Jaffe 1981; Murakami 1983; Augustine 1984; Albright et al. 1985; Meisner and Arkin 1987; Mapes and Houze 1993; Chang et al. 1995; Chen and Houze 1997; Sui et al. 1997), as well as through numerical modeling (e.g., Fingerhut 1978; Randall et al. 1991; Miller and Frank 1993; Xu and Randall 1995).

It is generally accepted that a diurnal cycle with a nocturnal–early morning convection maximum occurs over open oceans, while a diurnal cycle with an afternoon–evening maximum is prevalent over land. However, some distinct patterns of diurnal variations have been documented with striking geographic distinctiveness due to prevailing local circulations, topography, sea–land contrast, etc. For example, a number of observational studies showed an afternoon maximum in rainfall and cloudiness over tropical oceans (e.g., Gray and Jacobson 1977; McGarry and Reed 1978; Wexler 1983) and a nocturnal summer maximum rainfall over the central United States (e.g., Wallace 1975). Augustine (1984) reported that four of the five areas studied in the tropical Pacific Ocean display dual maxima, one near dawn and the other in midafternoon. This double peak behavior was also found over large tropical islands (Gray and Jacobson 1977). What is more, the phase and amplitude of the diurnal cycle is closely related to convective regimes. Gray and Jacobson (1977) indicated that the more intense the deep convection and the stronger the association with organized weather systems, the more significant the diurnal cycle with a maximum in the morning. Mapes and Houze (1993) and Chen and Houze (1997) noted that the amplitude of the diurnal cycle varies strongly with cloud cluster size.

Various mechanisms have been advocated to explain the observed diurnal convective variations. One plausible theory is based on the daily alteration of the low-level thermodynamics in response to the radiative heating cycle over land surfaces (Wallace 1975). The daytime solar heating increases the low tropospheric temperature and moisture (through increased evaporation) and thereby the thermal instability, creating the thermodynamic conditions most suitable for convection dur-

* The National Center for Atmospheric Research is sponsored by the National Science Foundation.

Corresponding author address: Dr. Changhai Liu, National Center for Atmospheric Research, P.O. Box 3000, Boulder, CO 80307-3000. E-mail: chliu@ncar.ucar.edu

ing afternoon–evening hours. By contrast, the nocturnal cooling through net infrared radiation enhances the static stability and thus suppresses convective activity. This thermodynamic argument has been commonly invoked to interpret the diurnal convective variation over land areas and large islands with an apparent surface heating cycle. Another attempt was made by Brier and Simpson (1969) to account for the observed semidiurnal cycle in terms of the semidiurnal pressure wave forced by the heating of ozone in the upper stratosphere. However, this theory suffers from serious limitations, as pointed out by Gray and Jacobson (1977), and fails to offer satisfactory explanations for the observed daily variability.

Two physical processes have been suggested as responsible for the pervasive diurnal cycle of deep oceanic convection featuring a late night or early morning maximum intensity. The first is referred as *direct radiation–convection interaction* (Randall et el. 1991). This hypothesis assumes that, during the day, solar warming in the convectively produced cloud shield acts to stabilize the atmosphere through reducing the temperature lapse rate and consequently restricts convective development; whereas, at night, the differential infrared cooling between the cloud base and cloud top creates a thermodynamic structure favorable for convective activity (Webster and Stephens 1980). The diurnal radiative cooling–heating cycle also affects the tropospheric relative humidity and available precipitable water and this has been recently hypothesized as the primary cause of the daily oceanic rainfall cycle (Tao et al. 1996; Sui et al. 1997). The second involves *cloud–cloud-free radiation difference,* proposed by Gray and Jacobson (1977). This hypothesis emphasizes the dynamical consequence of the differential radiative heating over the convective region and over the surrounding less cloudy (or clear) region. The net radiative cooling of cirrostratus at upper levels is greater at night and less during the day than in the adjacent environment. This situation is reversed at low levels. This day–night differential heating cycle tends to produce a daily variation in the horizontal divergence field and thus in convective activity.

It should be stressed that the foregoing physical processes are *in addition to* regional diurnal variation associated with terrain, sea–land breeze circulations, local flow characteristics, and certain types of weather systems. The character of daily variability in nature is further complicated by the remote impact of continents (Silva Dias et al. 1987; Randall et al. 1991), the internal dynamics (life cycles) of cloud clusters (McGarry and Reed 1978; Chen and Houze 1997), and sea surface temperature gradient and diurnal variability.

In this study we use a cloud-resolving numerical model to investigate this important phenomenon by concentrating on tropical deep precipitating convection over open oceans. In particular, emphasis will be placed on exploring the most general and basic physical aspects of the diurnal cycle through a series of idealized numerical experiments, rather than a case study or a real-time simulation approach. Our primary objectives are 1) to simulate the diurnal variations of tropical cloud systems, 2) to quantify the diurnal variations among convective regimes (i.e., highly organized cloud clusters vs less organized convection), and 3) to quantify the role of various physical processes in the diurnal variation.

The paper is organized as follows. In section 2 we give a brief description of the numerical model and experiment design, followed by effects of cloud organization in section 3; we present sensitivity to cloud-radiative forcing in section 4, followed by sensitivity to large-scale thermodynamical forcing in section 5; we compare the simulation results with observations and previous modeling studies in section 6 and evaluate principal hypotheses in section 7; and finally, we conclude with a summary in section 8.

2. Methodology

a. Model

We use a two-dimensional version of the anelastic nonhydrostatic cloud model developed by Clark and collaborators (Clark et al. 1996). The model utilizes second-order accurate numerics for both temporal and spatial terms in the momentum equations. The moisture, potential temperature, and hydrometeors (i.e., cloud water, rainwater, and ice) equations are solved with the multidimensional positive-definite transport algorithm. Rigid and free-slip boundary conditions are employed at the top and bottom of the model domain. Cyclic or periodic boundary conditions are implemented at the lateral boundaries. In addition, a Rayleigh friction ''sponge layer'' is imposed in the top 10 km to dampen the vertically propagating, convectively generated gravity waves that would otherwise be reflected in an unrealistic way. The absorber increases linearly in amplitude with height, starting from zero at the bottom of the sponge layer and reaching 0.001 at the top.

The two-dimensional domain spans an area 600 km long by 26 km high, with a constant grid interval of 2 km in the horizontal direction. The vertical coordinate is stretched with a grid length of 0.1 km at the lowest level and 1 km at the uppermost level. There are 56 vertical levels.

b. Physical parameterizations

The formulation of warm rain physics is based on the bulk parameterization of Kessler (1969). The ice phase microphysics uses the bulk parameterization of Koenig and Murray (1976), which has two types of ice. Type A represents particles that are formed by heterogeneous ice nucleation or ice splintering resulting from riming. Type B (graupel) denotes particles that are initially created by the freezing of rainwater. Each category is rep-

resented by two variables, namely, the mixing ratio and the number concentration. Currently, the ice growth processes in the model include 1) nucleation of type A by prescribed sorption nucleation spectra; 2) nucleation of type B by collision of type A with raindrops; 3) diffusion and sublimation of types A and B; 4) accretional growth of type A by the collection of cloud and rain water; 5) accretional growth of type B by the collection of cloud water and rainwater; and 6) melting of types A and B to rainwater.

The radiative transfer parameterization is the NCAR's Community Climate Model 2 (CCM2) scheme (Kiehl et al. 1994). In brief, the longwave radiative transfer is based on an absorptivity–emissivity formulation (Ramanathan and Downey 1986). The absorptivity and emissivity for CO_2 and O_3 are evaluated by the broadband technique, which assumes that the spectral range of absorption by a gas is limited to a relatively small range in wavenumber and hence can be calculated at the band center. The water vapor absorptivity and emissivity is estimated with the nonisothermal formulation of Ramanathan and Downey (1986). The cloud emissivity (ϵ) is given as $\epsilon = 1 - e^{-0.1\mathrm{LWP}}$ for all cloud types, where LWP (g m^{-2}) is the cloud water path.

The solar radiation model adopts a δ-Eddington scheme described by Briegleb (1992). The solar spectrum is divided into 18 discrete spectral intervals (7 for O_3, 1 for the visible, 7 for H_2O, and 3 for CO_2). Gaseous absorption by O_3, CO_2, O_2, and H_2O is treated by the exponential sum method. Cloud scattering and absorption employ the Slingo (1989) parameterization, which relates the extinction optical depth, the single-scattering albedo, and the asymmetry parameter to the cloud water path and the cloud drop effective radius.

Instantaneous quantities, including temperature, water vapor mixing ratio, and cloud hydrometeors, are utilized to calculate the radiation fluxes. The radiative heating–cooling is considered to be a slowly varying field. So, since the radiative scheme is computationally expensive, a large time step is adopted for the radiation calculation in most numerical simulations. This approach may be adequate in large-scale and mesoscale models. In cloud-resolving models, however, a small time interval should be used because shortlived individual convective cells can rapidly advect and are explicitly resolved. This is particularly true in a long time integration where errors may be cumulative and nonlinear. In our experiments, therefore, the radiation parameterization is activated at every time step.

The surface sensible heat and moisture fluxes are computed using a bulk aerodynamic formula, in which the exchange coefficients are functions of the bulk Richardson number (Deardorff 1972). The whole model domain is assumed to be over an open ocean with a constant surface temperature of 30°C, as commonly observed in the equatorial western Pacific warm pool region.

c. Experiment design

Starting from a horizontally homogeneous atmosphere, each experiment is initialized with a thermodynamic sounding typical of those observed during TOGA COARE (Tropical Ocean Global Atmospheric Coupled Ocean–Atmospheric Response Experiment) but with an idealized wind profile. Small potential temperature perturbations are randomly applied in the lowest model level to initiate convection. The large-scale forcing employed in our numerical experiments is a horizontally uniform, time-independent cooling and moistening due to the large-scale horizontal and vertical advection and other large-scale processes. This external forcing helps maintain vigorous convection in the periodic domain. As displayed in Fig. 1a, two different large-scale forcings are used. The first, labeled "S," represents a strong forcing with the maximum cooling of -10 K day^{-1} around 550 mb and the maximum moistening of 4 g kg^{-1} day^{-1} (equivalent to about 10 K day^{-1}) around 850 mb. The second, labeled "W," is identical to the previous one in shape but with half the magnitude.

The effect of environmental conditions, especially wind shear, on regimes of convection is a fundamental one, as dynamically quantified in Moncrieff (1981). On the one hand, a jetlike profile is conducive to squall line cloud systems whether or not large-scale forcing exists; on the other hand, large-scale ascent in an unsheared environment tends to energize nonsquall cloud clusters but does not necessarily much affect convective dynamics. Two kinds of large-scale wind fields are used to study the diurnal variation of convective regimes and are displayed in Fig. 1b. The first, labeled "U1," corresponds to the profile with a moderate low-level (from surface to 800 mb) shear and a reverse upper-level shear. This is used to generate a squall-line-type organized convective system typically observed in these conditions. The second, labeled "U2," corresponds to calm surroundings and is used to realize less organized nonsquall cloud clusters.

In the experiments with the sheared wind profile U1 in Fig. 1b, a relaxation term or large-scale momentum forcing is added to the horizontal momentum equation in order to maintain the low-level shear that would normally be maintained by large-scale processes but would otherwise be removed by small-scale circulations. This procedure helps maintain a long-lasting organized convective system in a periodic domain. It is defined as

$$\frac{\partial u}{\partial t} = \cdots - \frac{\overline{u} - U}{\tau},$$

where the variables $\overline{u}$ and U represent the horizontal wind component averaged over the entire model domain and the initial large-scale wind profile, respectively, and τ represents a timescale during which the model-predicted wind relaxes toward the specified environmental

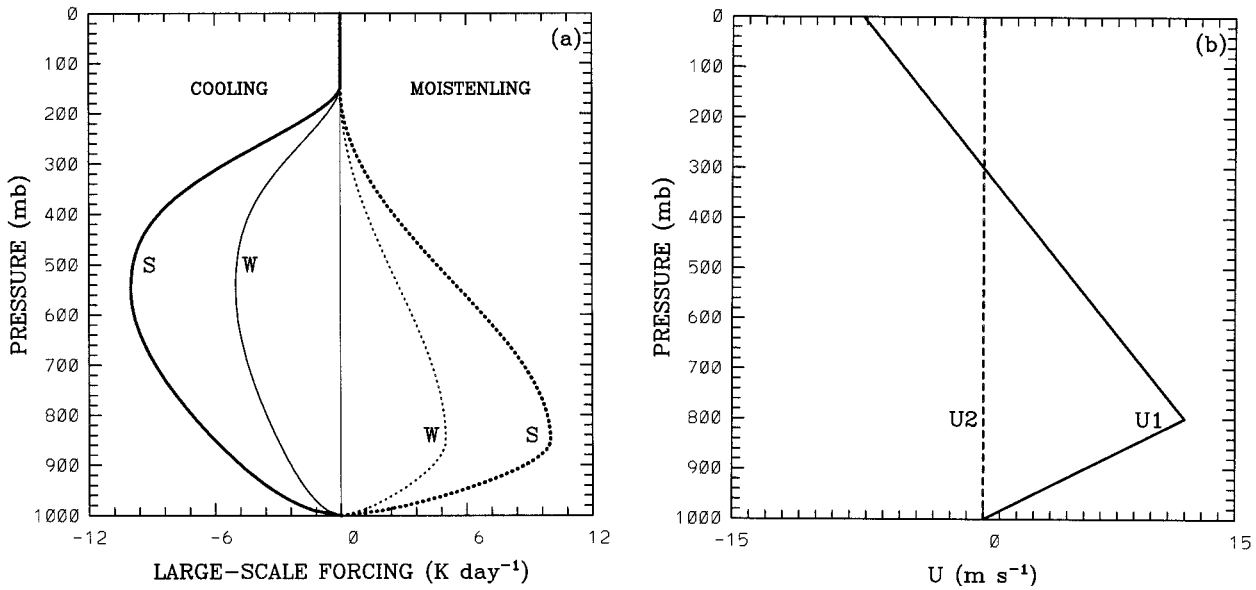

FIG. 1. (a) Large-scale cooling and moistening; (b) large-scale wind used for simulating highly organized squall lines (continuous line U1) and nonsquall cloud clusters (broken line U2).

wind. A value of 3 h is adopted in our experiments. This approach was previously employed in cloud-resolving modeling of tropical cloud systems during GATE by Grabowski et al. (1996).

A total of eight numerical experiments were conducted and are tabulated in Table 1. Each simulation starts from midnight at the local standard time (LST) and is carried out for 12 model-equivalent days. The initial thermodynamic profile arguably affects the simulation during the first couple of days but should not much affect the long-term statistical behavior, which is predominantly determined by the imposed large-scale forcing and the sea surface temperature. In order to minimize the effect of the specific initial field as well as the ''spinup'' of the modeled fields, we analyze only the last 10 days of integration in each simulation.

TABLE 1. A list of numerical experiments.

Experiment	Wind profile (Fig. 1b)	Momentum forcing	Cooling and moistening (Fig. 1a)	Fully interactive radiation
EX1	U1	on	S	yes
EX2	U2	off	S	yes
EX3	U1	on	S	no*
EX4	U2	off	S	no*
EX5	U1	on	W	yes
EX6	U2	off	W	yes
EX7	U1	on	S	no**
EX8	U2	off	S	no**

* The effect of cloud condensate on radiation is excluded.

** The radiation flux horizontally averaged over the model domain is applied at every grid point.

3. Effects of cloud organization

a. Persistent highly organized systems

The control experiment, corresponding to EX1 in Table 1, uses the idealized strong large-scale forcing and the sheared wind profile U1 in Fig. 1 and includes full microphysics, as well as fully interactive radiation and the large-scale momentum forcing. In response to the thermodynamic instability resulting from the moisture and sensible heat transports from the warm ocean surface, shallow cumulus convection initially developed randomly in the planetary boundary layer. After about 5 h into the simulation, in response to the large-scale destabilization, deep convection began to develop and subsequently evolved into several organized convective systems as illustrated by the time–space plot of surface precipitation in Fig. 2a. These convective systems either merged or dissipated; eventually, after about 1 day into the simulation, one well-organized mesoscale convective system dominated. Because of the steady thermodynamic forcing and momentum forcing, this single system persisted throughout the remaining 11 days of integration, albeit intermittent with relatively weak and less organized convection.

The structure of this convective system is illustrated by a snapshot of the total hydrometeor field (i.e., sum of cloud water, rainwater, and ice mixing ratio) in Fig. 3. It manifested the characteristic eastward-moving squall-line-like structure associated with the low-level jetlike wind profile. The system contained several convective cells at various stages of their life cycles—a multicellular structure typical of oceanic squall lines. Convective elements periodically formed along the

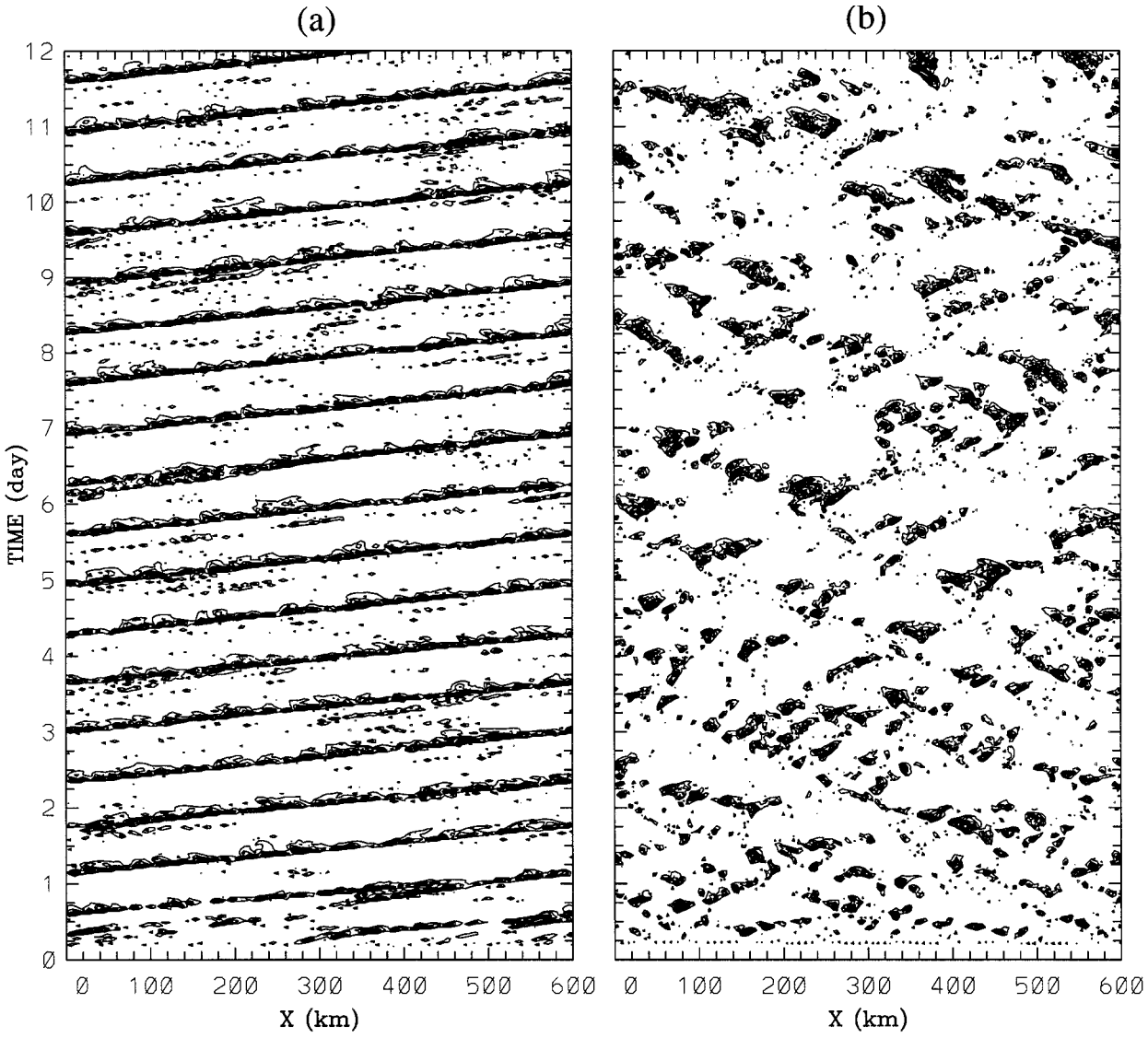

FIG. 2. Time–space plots of the surface precipitation rate for (a) EX1, which features squall lines, and (b) EX2, which features nonsquall cloud clusters. Contours start with 1 mm h^{-1} at an interval of 2 mm h^{-1}.

leading edge of the surface gust front (around 360 km) and thereafter advected rearward relative to the system, which is also typical. The active cloud reached an altitude of more than 15 km and the maximum vertical velocity was about 5.5 m s^{-1}. The trailing stratiform region was extensive, but no forward-directed anvil occurred because of the reversed low- and upper-level environmental wind shear. The entire system measured by the upper-level cloud deck was roughly 300 km long and moved eastward at a speed of approximately 10.5 m s^{-1}. The surface rainfall extended over 100 km rearward from the heaviest precipitation at the leading edge of the cloud system. Also noticeable were the less vigorous scattered convection and the inactive high cloud (convectively generated cirrus) surrounding the squall line.

Figure 4 presents the diurnal cycles of ensemble means of the domain-averaged precipitation rate, the maximum vertical velocity, and the total condensate. Herein, the ensemble mean was defined as the average with respect to LST during the last 10 days. The time-averaged diurnal variation in Fig. 4a exhibited relatively stronger precipitation during the night and early morning (2100~0700 LST) and relatively weaker precipitation in the afternoon and evening (1100~1900 LST). A salient maximum existed around 0500 LST and the afternoon minimum occurred around 1530 LST. The difference between the maximum and the minimum rainfall rate was roughly 0.35 mm h^{-1}. This was about 40% of the daily mean value (0.86 mm h^{-1}). Note that the ensemble average not only removed the high-frequency variability, but also considerably smoothed the amplitude of the diurnal variation.

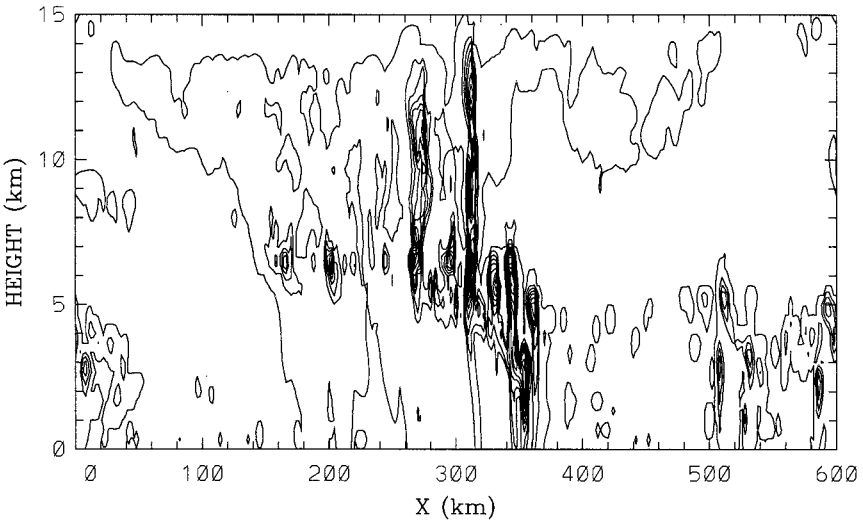

FIG. 3. Snapshot of the hydrometeor field at 100 hours in EX1. Contours start with 0.01 g kg^{-1} at an interval of 0.5 g kg^{-1}.

The ensemble means of the maximum vertical velocity (Fig. 4b) and total cloud condensate in the whole domain (Fig. 4c) indicated a notable diurnal modulation similar to the behavior of the mean precipitation. This resemblance arises because all these parameters are indicators of convection intensity. The upward velocity component showed that the diurnal variation calculated as the early morning maximum minus the afternoon minimum exceeded 2.5 m s^{-1}, approximately 43% of the daily mean intensity 5.8 m s^{-1}. In comparison with other parameters, the maximum vertical velocity contained much stronger high-frequency fluctuations. The total hydrometeor content displayed a predawn peak value, but the afternoon minimum was not obvious. The corresponding diurnal variation was 1.3×10^5 kg, equal to 20% of the daily mean value 6.5×10^5 kg. The correlation among the behavior of the precipitation, peak upward velocity component, and total hydrometeor was remarkable.

Figure 5 shows time–height cross sections of selected deviation fields. These are obtained by first taking both spatial and temporal average with respect to LST and then deducting mean values at each level. It should be pointed out that the modeled atmosphere tended to become warmer and moister relative to the initial state and this trend was removed in the time–height cross sections to depict the daily variability more clearly. The potential temperature (Fig. 5a) underwent a significant diurnal modulation characterized by negative anomalies (cooler) throughout the troposphere from midnight to noon and positive anomalies (warmer) during the remaining hours of the day. The diurnal variation was confined to the levels above 8 km due to the presence of extensive cirrus clouds (see later discussion) and their interactions with radiation, and it was virtually negligible at low levels. The most negative anomaly occurred at the height of 12.5 km around 0630 LST, and the positive peak centered at almost the same altitude around 1630 LST. The difference between the maximum and the minimum was more than 2 K. This is large for the tropical atmosphere, which usually has small horizontal variability.

The water vapor mixing ratio field (Fig. 5b) below 8 km was dominated by negative (drier) anomalies from 0000 to 1400 LST and positive (more moist) anomalies during other times. The most prominent diurnal variability took place at middle levels with a value of 0.2 g kg^{-1}. The diurnal variability at upper levels was minimal and obviously had a different phase. In comparison with the diurnal cycle in convective activity (Fig. 4), it is evident that the atmosphere became relatively dry when convection was most active and relatively moist when convection was suppressed. The dry episode is consistent with the action of convectively induced subsidence and the moist episode with the action of mean environmental ascent (large-scale forcing).

Our simulated results can be compared with previous studies. For instance, with a one-dimensional model Randall et al. (1991) found a broadly similar day–night variability in the potential temperature field. With a cumulus ensemble model Xu and Randall (1995) also obtained a comparable daily temperature variation except that the amplitude in the upper troposphere was much smaller and the lowest temperature appeared about 2.5 h earlier in their simulation. The observation in the GATE area (Albright et al. 1981) revealed a late-night minimum and an early afternoon maximum in the temperature field, and thus the timing of the lowest and highest temperature differs from that simulated in Fig. 5a. The observed specific humidity was marked by a daytime drying and a nocturnal moistening, clearly related to the diurnal convective cycle that had an after-

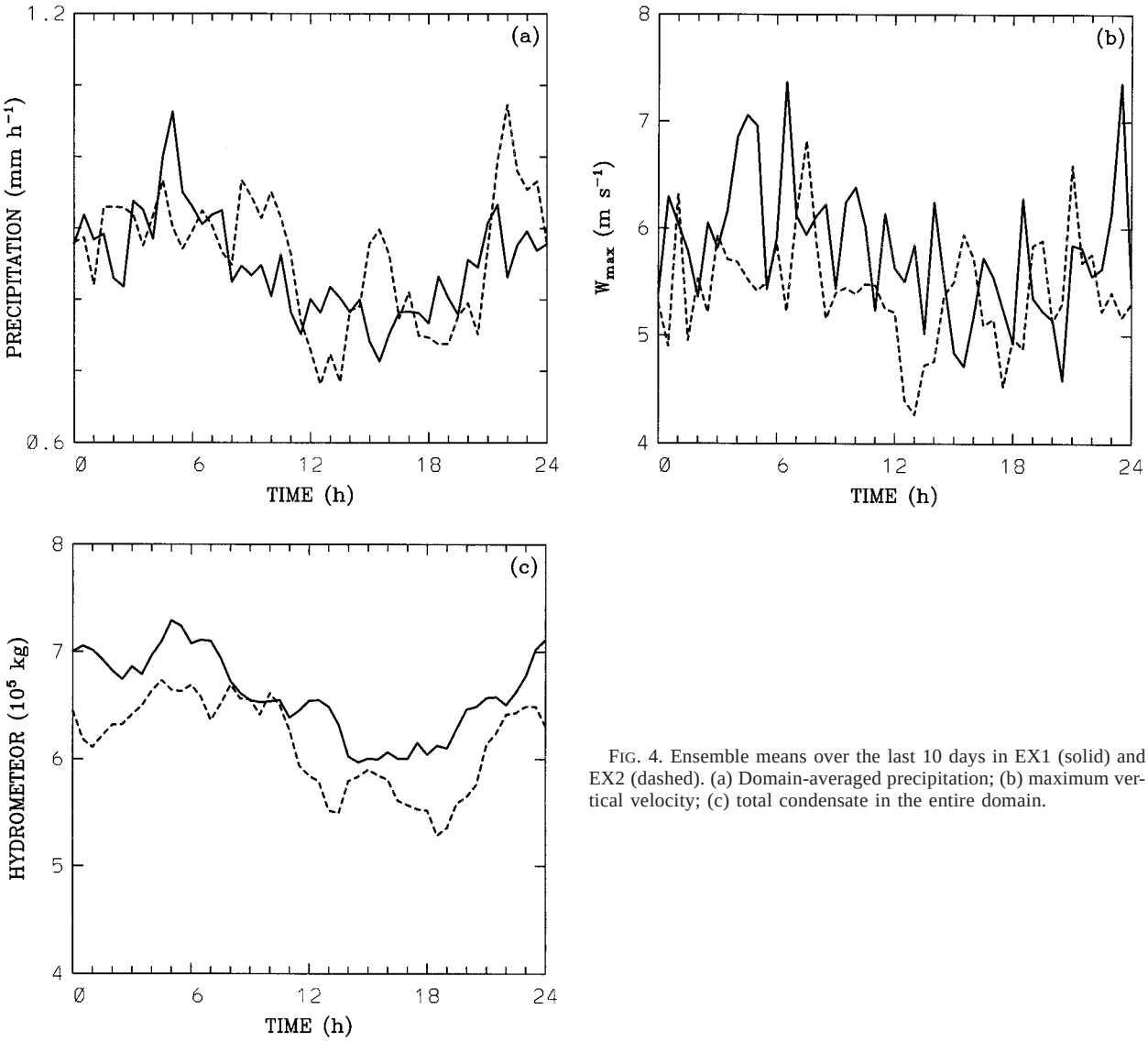

FIG. 4. Ensemble means over the last 10 days in EX1 (solid) and EX2 (dashed). (a) Domain-averaged precipitation; (b) maximum vertical velocity; (c) total condensate in the entire domain.

noon maximum intensity and was opposite to the pattern in Fig. 4a.

There was a 5-h phase difference in the low- and upper-level upward mass transports (Fig. 5c). The above-normal upward mass flux was most obvious from 0200 to 1000 LST below 6 km, while it persisted during the night and entire morning above 6 km; the below-normal mass transport prevailed in the afternoon at low levels and in the late afternoon and evening at upper levels. As expected, the mass flux field was well correlated with the surface precipitation.

In the condensate field (Fig. 5d), the negative anomaly was widespread during the daytime and the positive anomaly was prevalent during the nighttime for the warm cloud below the melting level. For the ice cloud, the negative anomaly was most significant in the afternoon and the evening, and the positive anomaly dominated during the remaining time. The phase lag between the diurnal variations of the high and low clouds was similar to that in the mass flux field. The diurnal variation displayed a double maximum in the vertical distribution: one located at 6 km and another above 10 km. These two peaks were closely linked to the cloud distribution, as will be described later.

b. Transient weakly organized (nonsquall) cloud clusters

The control experiment EX1 was designed to model a squall line type of organized convection. To examine the sensitivity of the diurnal variation to a different convective regime, a simulation with a motionless initial state, called EX2, was conducted. Another difference between this experiment and EX1 is that the horizontal

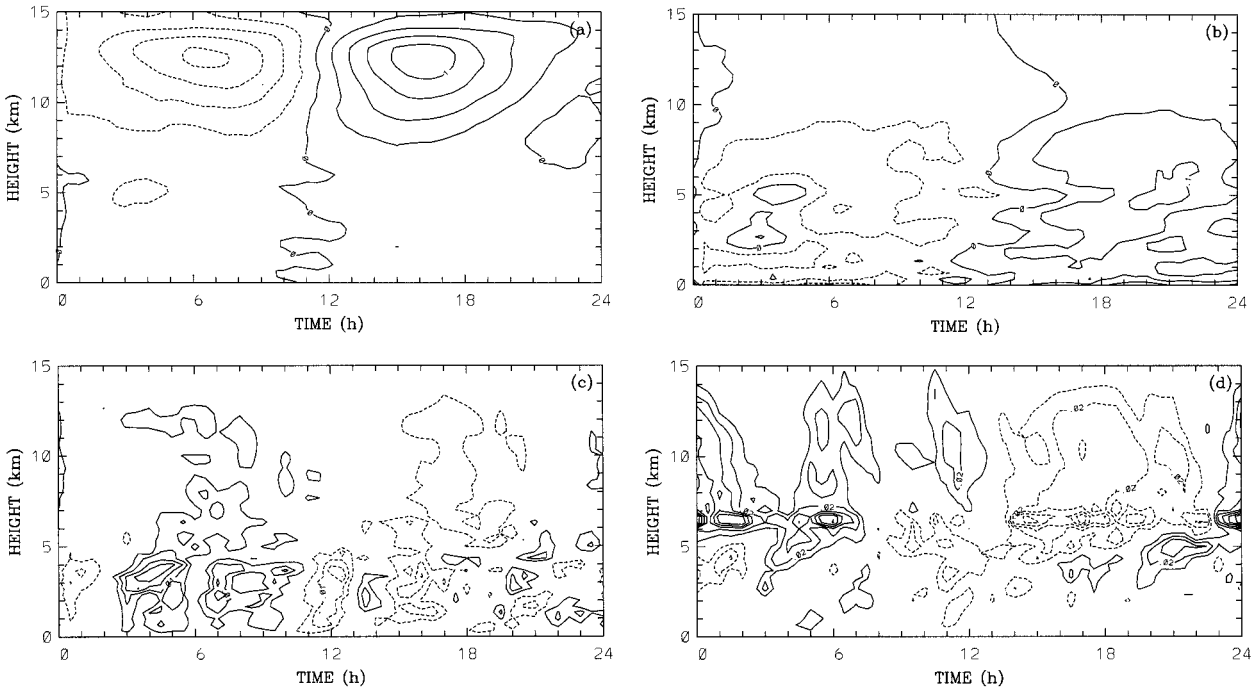

FIG. 5. Time–height cross sections of diurnal anomalies (with respect to the mean at each level) averaged during the last 10 days in EX1 (positive values solid, negative values dashed). (a) Potential temperature (0.25-K intervals); (b) water vapor mixing ratio (0.05 g kg^{-1} intervals); (c) upward mass flux (0.005 kg m^{-2} s^{-1} intervals; zero line omitted); and (d) total condensate (0.01 g kg^{-1} intervals; zero line omitted).

momentum forcing was deactivated. Although a weak nonzero mean wind field was established during the integration, the domain-averaged wind profile did not develop a systematic low-level shear. As a consequence, long-lived organized mesoscale convection did not occur. Instead, several relatively short-lived precipitating convective systems coexisted during most of the integration, as evinced by the time sequence of surface rainfall rate over the domain in Fig. 2b. The structure of these less organized cloud systems is exemplified by a snapshot of the total hydrometeor field in Fig. 6. In terms of the upper-level cloud decks, these convective systems ranged in horizontal extent from a few kilometers to a few tens of kilometers, and they had a lifetime ranging

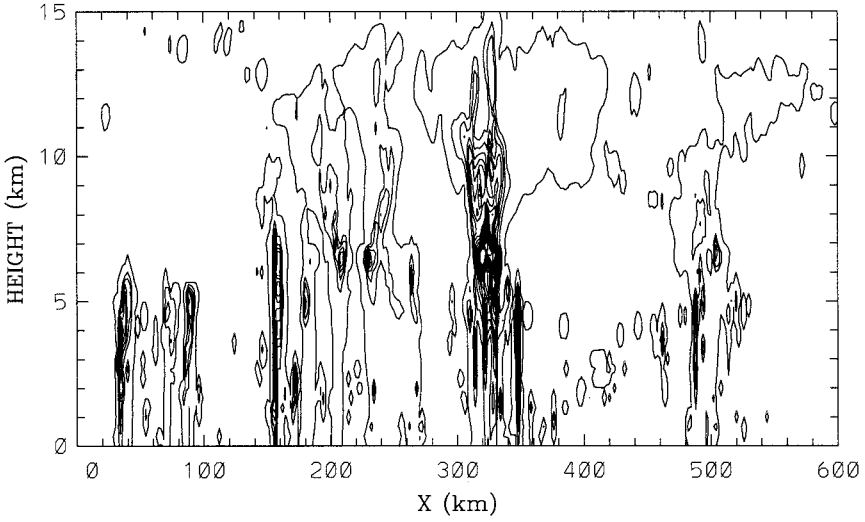

FIG. 6. Snapshot of the hydrometeor field at 100 hours in EX2. Contour starts with 0.01 g kg^{-1} at an interval of 0.5 g kg^{-1}.

from 1 h to more than 10 h. (The longer-lived cloud systems could be called ''nonsquall'' clusters). Additionally, the precipitation distribution in Fig. 2b reveals that convective systems tended to increase in horizontal scale and be longer lasting in later stages of the integration. This was due to the development of *local* shear. Note that the squall line system in Fig. 3 is ''coherent'' in the sense that it consists of a closely coupled series of propagating convective cells embedded in a mesoscale system. On the other hand, convection in Fig. 6 is essentially a series of weakly coupled transient cells of a cumulus congestus (a nonsquall type). This dynamical distinction is very clear in the time–space plot of surface rainfall (Fig. 2). Notably, the convection did not evolve into into a single mesoscale system, in contrast to EX1. This suggests that the EX1-type evolution is physically based and shear dependent, and it is not an artifact of the periodic boundary conditions.

The ensemble average of surface precipitation rates over the last 10 days of simulation displayed a noticeable diurnal cycle with heavier precipitation occurring during the night and early morning (2130~1100 LST) and lighter precipitation in the afternoon and evening (Fig. 4a). Because of the equal large-scale forcing and comparable surface heat and moisture fluxes, the mean precipitation in EX2 was almost identical to that in EX1. The diurnal variation measured in terms of the difference between the peak precipitation and the precipitation minimum was also comparable to the control experiment, but the lowest precipitation occurred 3 h earlier and the predawn peak was absent in EX2. Another noticeable difference from EX1 concerned the existence of a dual minima in EX2: the major one in the early afternoon and the minor one in the evening.

The diurnal variation in the maximum vertical velocity and total condensate (Figs. 4b,c) displayed a pattern similar to that in the precipitation. In terms of the maximum vertical velocity, convection in EX1 was slightly stronger than in EX2 (5.8 vs 5.4 m s^{-1}). The hydrometeor amount was consistently larger all day in the control experiment than in EX2 (6.5×10^5 kg vs. 6.1×10^5 kg), even though their diurnal cycles bore an overall qualitative similarity. As a consequence, the precipitation efficiency, defined as the ratio of precipitation to condensate, was greater because of the negligible difference in precipitation rates. This is in agreement with the finding by Ferrier et al. (1996) that the precipitation efficiency is a function of wind shear. In other words, the storage of water in the atmosphere is larger if the convection is more organized.

Time–height cross sections of physical deviation fields (not shown) displayed many similarities to Fig. 5. As in the control experiment, the diurnal modulation in the potential temperature centered in the upper troposphere. Moreover, both the timing and intensity of extreme potential temperature perturbations were comparable in the two experiments. These striking resemblances were intimately related to the similar cloud structure (see later discussion). An identifiable difference in the water vapor field from EX1 was that the upper-level positive deviation in EX2 persisted from the midafternoon until dawn. The differences in the mass flux and condensate fields are fundamentally linked to the difference in precipitation patterns between the two experiments. For example, there are two negative anomaly centers in the early afternoon and the evening, respectively, well correlated with the double precipitation minima in EX2 (see Fig. 4).

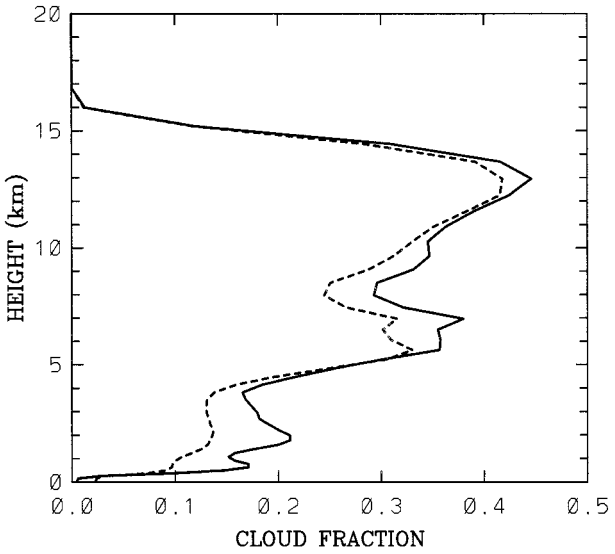

FIG. 7. Vertical distribution of the fractional cloudiness averaged over the domain and during the last 10 days in EX1 (solid line) and EX2 (dashed line).

Figure 7 portrays the space- and time-averaged vertical distribution of the cloud fractions. In the calculations, a cloud amount of 100% is assumed in a grid box when the sum of cloud water and cloud ice mixing ratios exceeds 0.01 g kg^{-1}. When this height-independent criterion was utilized, the estimated cloud spectrum in EX1 exhibited triple peaks, indicative of three main cloud population types. The cloud fraction maximum of around 0.2 in the lowest 2 km corresponded to the shallow boundary layer cumulus clouds; the maximum of about 0.38 was located near the melting level; the maximum of approximately 0.45 corresponded to deep cumulonimbi and stratiform clouds. The cloud cover displayed a similar spectrum, but it was less extensive throughout the troposphere in EX2 than in the control experiment. In particular, the low-level peak was absent and the midlevel peak was roughly 85% of its counterpart in EX1. The greater cloudiness in the control experiment was consistent with the greater hydrometeor content in Fig. 4c. It is contributed to the jetlike ambient wind, which is beneficial to the formation of extensive stratiform cloud decks through the movement of convective cells and hydrometeors rearward relative to the leading edge of the squall system. It should be mentioned that the estimation of cloud amount strongly de-

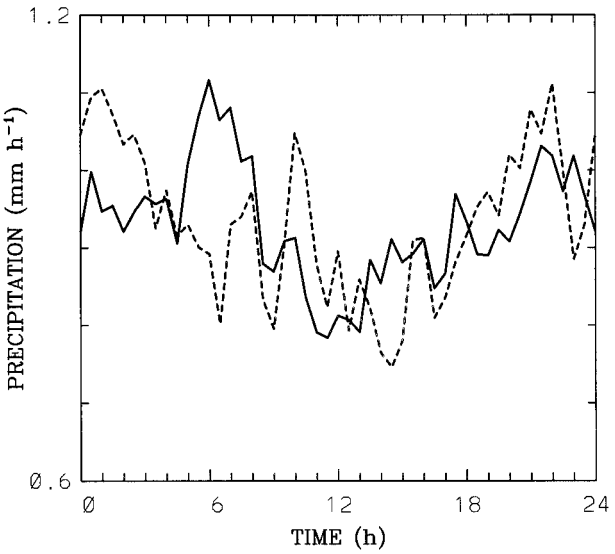

FIG. 8. Ensemble means of the domain-averaged precipitation over the last 10 days in EX3 (solid) and EX4 (dashed).

pends upon the subjectively specified criterion. For example, the high-level cloudiness was enhanced and the corresponding peak was shifted upward, whereas the low-level cloud fraction was substantially reduced upon using a height-dependent threshold that is proportional to the saturation water vapor mixing ratio as in Xu and Krueger (1991) (not shown). The cloudiness may also be influenced by the microphysical formulation used in the model.

4. Sensitivity to cloud-radiation forcing

EX3 and EX4 are same as EX1 and EX2, respectively, except that all radiative effects of clouds, or cloud-radiative forcing, were omitted by setting the liquid and ice water path to zero in the radiation scheme. These radiatively ''cloud-free'' experiments are used to investigate what kind of diurnal variability occurs when the interaction between the convectively generated cloud and radiation is ignored. As in the control experiment, a well-organized convective system developed and persisted throughout the simulation EX3. In EX4, convection was relatively less organized like EX2. The convection in both experiments was stronger than in their fully radiatively interactive counterparts in terms of the maximum vertical velocity and surface precipitation intensities, suggesting that the net impact of clouds on radiation (viz., cloud radiative forcing) acted to weaken the convective activity. The character of the diurnal precipitation variation in EX3 (Fig. 8) was (statistically speaking) comparable to EX1 (Fig. 4). The above-average precipitation occurred in the night and early morning with a peak at 0600 LST. EX4 was generally characterized by a larger nocturnal precipitation and less daytime precipitation. However, we will show later that the operating physical processes for the modeled diurnal cycle differ.

In contrast with the negative feedback on rainfall, the cloud-radiative forcing was found to have a strong positive feedback on the upper-level clouds, namely, it increased the fractional cloudiness but had little impact on the mid- and low-level clouds (Fig. 9). This result suggests that the cloud-top cooling and cloud-bottom warming due to cloud infrared radiative interactions (Webster and Stephens 1980) enhance the stratiform circulation. However, the cloud solar radiative interaction could reduce the upper-level circulation through the cloud-top warming. Nevertheless, the cloud infrared radiative forcing dominated the cloud solar radiative forc-

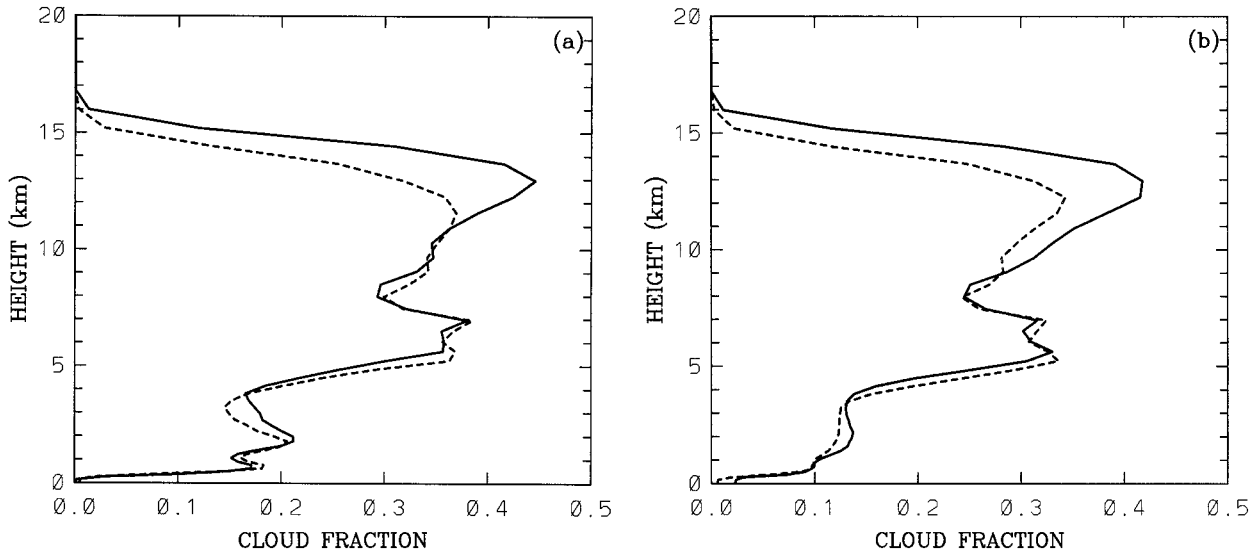

FIG. 9. Vertical distribution of the fractional cloudiness averaged over the domain and during the last 10 days of simulation: (a) EX1 (solid) and EX3 (dashed); (b) EX2 (solid) and EX4 (dashed).

ing in our simulations, at least as far as the anvil cloudiness was concerned. Another interesting point is the greater cloudiness throughout the troposphere in EX3 compared to EX4.

Fu et al. (1995) and Tao et al. (1996) examined the cloud-radiative forcing in tropical squall cloud clusters with cumulus ensemble models by performing two numerical simulations. One included fully interactive radiative heating and the other only the clear-sky radiative heating computed from thermodynamic profiles either at a fixed grid point (Fu et al. 1995) or averaged over the domain (Tao et al. 1996). Both studies revealed that the cloud radiative forcing suppresses convective activity and decreases surface rainfall but increases the longevity of anvil cirrus and cloud cover in the troposphere, a conclusion that agrees with our results. Note that both Fu et al. (1995) and Tao et al. (1996) concentrated only on infrared radiation.

Dudhia (1989) performed analogous experiments using a hydrostatic mesoscale model but with *parameterized* cumulus convection. He found that the simulated convective system in the absence of cloud-radiative forcing is very similar to that including cloud-radiative interaction except that the cirrus extent is greatly reduced, consistent with our cloud-resolving simulations.

Using a general circulation model with an ocean-covered earth (''Seaworld''), Randall et al. (1989) conducted a pair of simulations with and without cloud effects in both the solar and terrestrial radiation parameterization to explore the influence of cloud radiative forcing. The simulation including the cloud-radiation interaction produces about 15% more global precipitation, which is opposite to our finding. The difference is highly likely to be due to the fundamental distinction between the feedback in general circulation models and the cloud-resolving models. In cloud-resolving models, explicit redistribution of water vapor and condensate can interact with radiation on small spatial and temporal scales. This is distinct from general circulation models, where the smallest resolved scale of interaction is the grid scale, which is typically several hundred kilometers.

5. Sensitivity to large-scale forcing

Two experiments (EX5 and EX6) were carried out with the weak forcing shown in Fig. 1a in order to examine the sensitivity of the modeled diurnal cycles to the strength of the cooling and moistening due to changes in the large-scale advection. Like the control experiment, the simulated convection in EX5 featured the squall-line-like regime, which was intermittent with less organized convection. The convective behavior in EX6 was, for the most part, similar to that in EX2. As expected, and in agreement with Tao and Simpson (1984), weak large-scale forcing produced weaker convection and less precipitation. However, the reduction in precipitation in both simulations was less than the 50% reduction in the large-scale forcing. The ensemble means of surface precipitation in Fig. 10 showed a diurnal variation resembling the counterpart with the strong forcing. EX5 was characteristic of a peak precipitation at 0530 LST and a lowest precipitation at 1730 LST. In EX6, above-average precipitation prevailed during the night and morning and below-average precipitation occurred in the afternoon. The difference between the maximum and minimum in EX5 was roughly 0.27 mm h^{-1}, less than that in the control experiment, but the diurnal variation relative to the 24-h mean was more than 50%, greater than in the control experiment. The same was true of EX6. These results illustrate that the simulated diurnal cycle was a robust feature that did not strongly depend on the large-scale forcing.

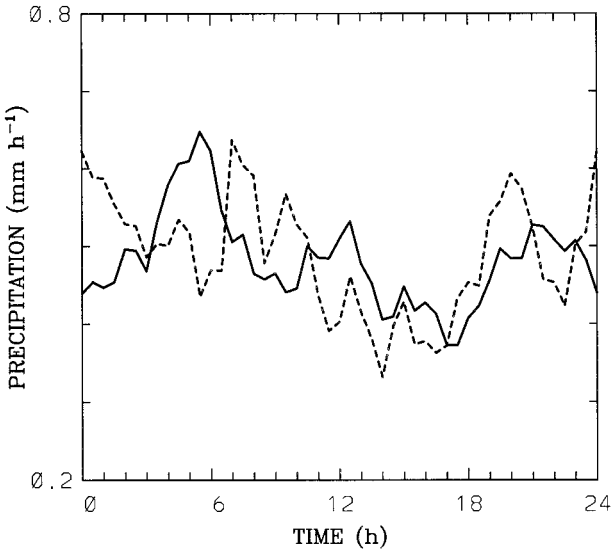

FIG. 10. Ensemble means of the domain-averaged precipitation over the last 10 days in EX5 (solid) and EX6 (dashed).

6. Comparison with observations and other modeling studies

Many observations have documented the existence of nocturnal or early morning maximum precipitation and convective activity over the oceans, free from the complicating influence of continents and large islands, in support of our modeling results. For example, Gray and Jacobson (1977) analyzed the 13-yr hourly precipitation data in western Pacific and found a salient peak around sunrise and an evening minimum for small-island stations. Using satellite and in situ data, Janowiak et al. (1994) showed the preference for predawn oceanic heavy rainfall and convective activity. Chang et al. (1995) derived annual mean rainfall maps based on satellite measurements and found that the morning rainfall is larger than the afternoon by about 20% over the oceanic region between 50°S and 50°N. The 24-h harmonic indicates a nocturnal or early morning maximum in

35%~40% of the oceanic region. Recently, Sui et al. (1997) analyzed diurnal variations over the equatorial Pacific warm pool region based on data collected during intensive observation periods of TOGA COARE. Their results reveal that the diurnal variation is dominated by heavier rain during the night from 2200 to 0600 LST and lighter rain in the remaining part of the day during the large-scale disturbed periods.

Our results are also in broad agreement with previous numerical studies. With a general circulation model, Randall et al. (1991) simulated an early morning maximum precipitation over the oceans far from land. Further experiments indicate that the same kind of oceanic diurnal cycle occurs even in the absence of neighboring continents and radiation effects of clouds. Experiments with a single-column version of the same general circulation model also produces a diurnal cycle of precipitation with a morning maximum. In the simulation of tropical cloud clusters with a two-dimensional mesoscale model, Miller and Frank (1993) obtained above the 24-h average rainfall between 2100 and 1200 LST and below-average rainfall during daytime hours. Xu and Randall (1995) performed two-dimensional explicit simulations of cumulus ensembles with prescribed large-scale advective effects, as in our study. The modeled convection is generally more intense during the nighttime than during the daytime, and the filtered rainfall shows the maximum in the early morning and the minimum in the early afternoon.

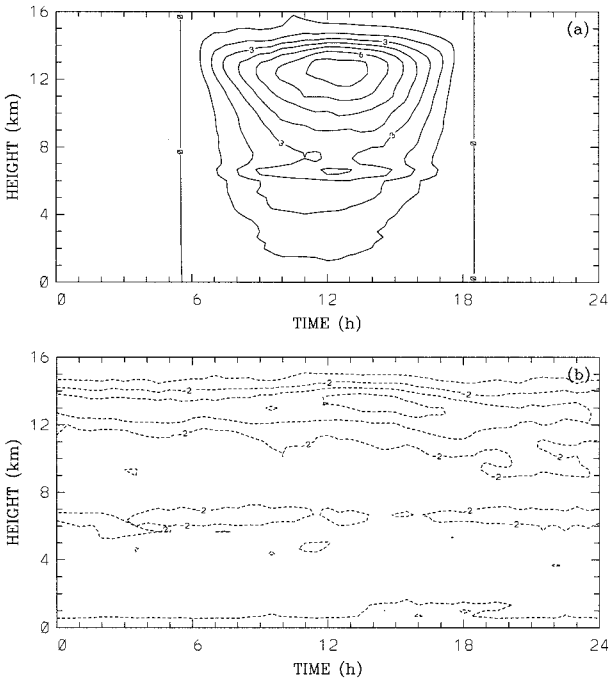

FIG. 11. Time–height cross sections of radiation fluxes averaged over the domain and over the last 10 days (with respect to LST) in EX1 (the unit is K day^{-1}). (a) Shortwave radiation; (b) longwave radiation.

7. Evaluation of principal hypotheses

Among the various mechanisms reviewed earlier, two particular radiative arguments are potentially relevant to the simulated diurnal cloud system cycle. The first concerns direct radiation–convection interaction, which is the stabilization due to the insolation absorption inside clouds during the day and the destabilization due to the infrared radiative cooling of cloud tops at night. The temperature deviation field in Fig. 5a illustrates that this argument is basically valid. The atmospheric stratification in the troposphere underwent a diurnal modulation with the strongest static stability in the late afternoon and the weakest stability in the early morning. This is consistent with the diurnal convective cycle. Note that the variability in the tropospheric static stability was mainly correlated with the diurnal variation in the upper-level temperature field, whereas the low-level temperature alteration was quite weak and made a minimal contribution. This situation was also true in EX2.

However, temperature variations represent a dynamical coupling among radiation, large-scale forcing, latent heating, and other physical processes. To isolate the effect of radiation on the atmospheric stratification, Fig. 11 presents the ensemble means of domain-averaged solar and longwave radiative fluxes over the last 10 days of the control simulation. The solar heating exhibited two obvious peaks in the vertical distribution: one located around 13 km with a value of 7 K day^{-1} and another around 6.5 km with a value of 4 K day^{-1} (Fig. 11a). This bimodal behavior is closely connected to the cloud spectrum distribution in Fig. 7. Obviously, the upper-level solar heating accounted for the positive potential temperature departure in the afternoon, and it is understandable that the former preceded the latter by several hours. The shortwave radiative warming enhanced the atmospheric static stability in the troposphere; it thus acted to inhibit the daytime convection. The longwave radiation cooled the entire troposphere and showed a weak diurnal variability (Fig. 11b). In the vertical, the longwave radiation cooling also displayed a bimodal structure with peaks located at almost the same altitudes as the solar radiation warming; the maximum upper-level and midlevel cooling rates reached as large as 4 K day^{-1} and 2 K day^{-1}, respectively. The total radiative fluxes (not shown) characterized a heating within the middle and upper troposphere from 0800 to 1600 LST and a cooling during most of the remaining time. In comparison with the potential temperature in Fig. 5a, it is readily seen that the daily radiative cooling–heating was partially canceled by other processes so that the thermal stratification experienced a negligible diurnal variability at the low and midlevels. Similar diurnal and vertical variations were found in EX2.

The second mechanism concerns the dynamical adjustment to the horizontal radiative heating gradient be-

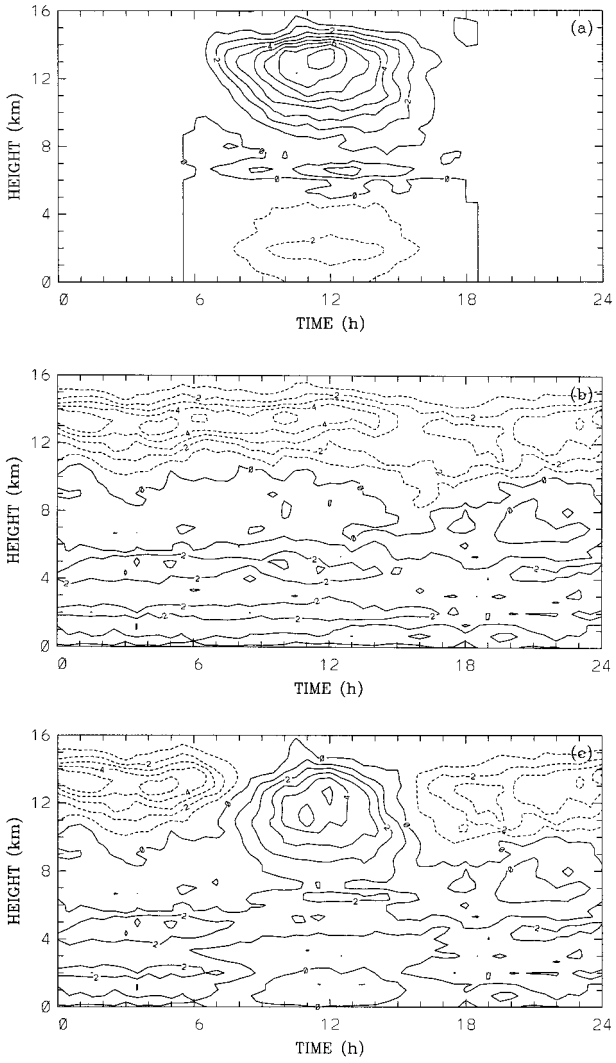

FIG. 12. Radiative heating difference (cloudy minus clear) in K day^{-1} averaged with respect to LST over the last 10 days in EX1. (a) Shortwave radiation; (b) longwave radiation; (c) total radiative fluxes.

tween cloudy and adjacent clear (or partly cloudy) areas of convective systems, simply called radiation–dynamics–convection interaction by Randall et al. (1991), or ''cloud–cloud-free radiative difference'' by Miller and Frank (1993). Gray and Jacobson (1977) argued that, relative to the environment, the cloud deck experiences enhanced infrared radiative cooling at night and solar warming during the day. An opposite radiative cooling–heating contrast occurs underneath the cloud shield. This inhomogeneous radiative cooling–heating creates a diurnal cycle in the mass divergence and vertical velocity profiles, which, in turn, can drive a diurnal cycle of convective activity. This hypothesis is supported by some observations (McBride and Gray 1980) as well as numerical simulations (Fingerhut 1978). Figure 12 presents the ensemble-mean differences of radiative fluxes between the cloudy region and the clear region. For simplicity, the cloudy region was defined as where the total liquid and ice water path integrated vertically from the model domain top to the planetary boundary layer top exceeded 0.4 kg m^{-2}. This procedure excluded the shallow cumulus cloudy area and the thin inactive cloudy area. A clear region was defined as one where the total water path was less than 0.1 kg m^{-2}. It is readily seen that the presence of cloud shields greatly altered the radiative energy absorption (Fig. 12a). The solar heating in the cloudy region was much larger above 6 km, with a peak value of 8 K day^{-1} near the cirrus cloud top, whereas it was 1–3 K day^{-1} less in the lower troposphere. The difference of the infrared radiation cooling was almost the opposite (Fig. 12b). The cooling in the cloudy region was 1–5 K day^{-1} stronger above 10 km but about 1–3 K day^{-1} weaker below 6 km. The total radiative fluxes in Fig. 12c showed that the cloudy region underwent more upper-level heating and more low-level cooling relative to the surrounding clear area during the day; this situation was just reversed at night. Therefore, the explicitly resolved cumulus convection results did lend support to Gray and Jacobson's hypothesis.

The key question is which of the above two mechanisms was the major player in our simulated diurnal variation? To address this problem, we conducted two further sensitivity experiments (EX7 and EX8), in which horizontally uniform radiative fluxes (determined as a domain average) were applied to the grid points at every time step to exactly eliminate the cloud–cloud-free radiation difference. The ensemble mean surface precipitation is shown in Fig. 13. It is striking that these simulations produced a diurnal cycle comparable to their counterparts with the fully interactive radiative transfer, albeit with differences in detail. These results imply that radiation–dynamics–convection interaction played a secondary role in the simulated diurnal cycle compared to direct radiation–convection interaction. This is consistent with the results reported in previous numerical modeling studies (e.g., Randall et al. 1991; Miller and Frank 1993; Xu and Randall 1995; Tao et al. 1996).

Other mechanisms in the simulated diurnal variability may be also operative. Among them is the diurnal variation of tropospheric relative humidity or available precipitable water in response to the radiative cycle (Tao et al. 1996; Sui et al. 1997). The nocturnal longwave cooling can increase the large-scale environment's relative humidity, allowing condensation to take place easily and making more available precipitable water [defined as the product of a reference relative humidity and the difference between the vertically integrated saturation water vapor amount and a reference value; see Sui et al. (1997) for details]. On the other hand, the daytime solar heating compensates for the effect of longwave cooling and leads to a less humid troposphere. Such a

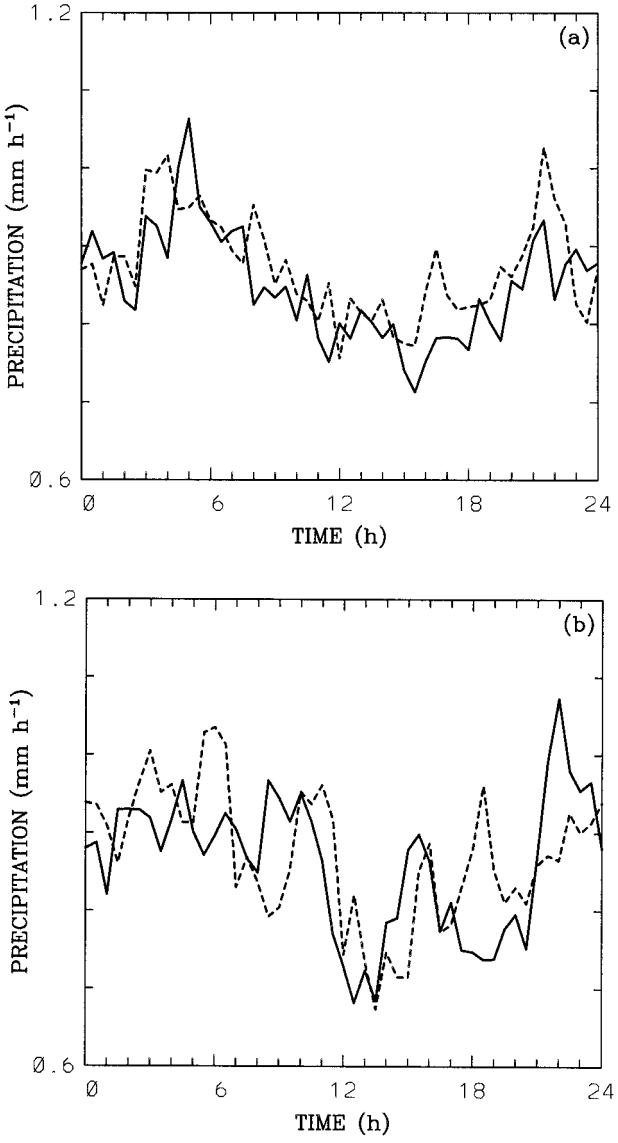

FIG. 13. Ensemble means of the domain-averaged precipitation during the last 10 days: (a) EX1 (solid) and EX7 (dashed); (b) EX2 (solid) and EX8 (dashed).

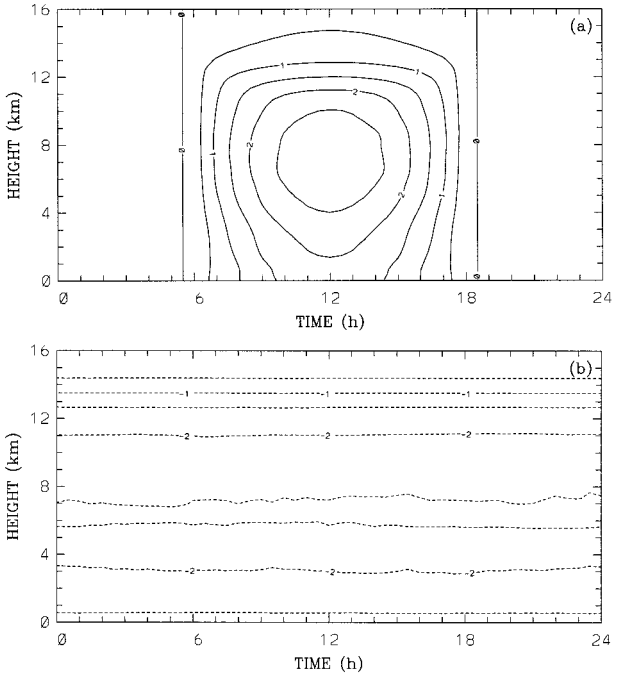

FIG. 14. Time–height cross sections of radiation fluxes averaged over the domain and over the last 10 days (with respect to LST) in EX3 (the unit is K day^{-1}). (a) Shortwave radiation; (b) longwave radiation.

sun-synchronous change in relative humidity could play a part in the simulated convective cycle.

Diurnal radiative heating and cooling can also influence day–night convective variations through the action of gravity waves. As discussed above, due to cloud-radiation interactions, a prominent diurnal modulation in the static stability took place in the upper troposphere. This static stability cycle can affect the vertical propagation of gravity waves, which, in turn, may affect cloud organization and its diurnal variability (Tripoli and Cotton 1989a,b)

Neither the direct radiation–convection interaction nor the cloud–cloud-free radiation difference discussed earlier can account for the diurnal cycle in the experiments without cloud-radiation interactions. Figure 14 portrays the time–height distribution of radiation fluxes averaged over the domain and the last 10 days in EX3. The solar radiative heating attained an extremum of 2.5 K day^{-1} in the middle troposphere (Fig. 14a). In comparison with the control experiment that includes fully interactive radiation (Fig. 11a), it is obvious that the low-level warming (below approximately 6 km) was moderately strengthened while the upper-level warming was dramatically weakened in the absence of the cloud blocking of solar radiation. Clearly, the solar heating contributed to raising the static stability within the low troposphere and to reducing the tropospheric relative humidity and the surface fluxes, thus suppressing the daytime convection. The infrared radiation showed little diurnal variation, characteristic of a 1.5~2.5 K day^{-1} cooling in most of the troposphere (Fig. 14b).

8. Conclusions

A two-dimensional nonhydrostatic cloud-resolving model was used to examine the diurnal variation of tropical oceanic convection under the conditions of horizontally uniform, time-independent large-scale forcing and sea surface temperature. The experiment design eliminated many extraneous factors that influence regional daily variability, for example, topography, sea–land contrast, and time-varying forcing and sea surface temperature. This study is aimed at exploring basic and

general physical processes controlling the diurnal variation that existing observational datasets cannot address in a systematic way.

When the full microphysics and fully interactive radiations were included, the modeled convection displayed a significant diurnal cycle characterized by a nocturnal and early morning heavier precipitation and an afternoon–evening lighter precipitation, which agrees with many previous observations. By comparison, the highly organized case had a more pronounced predawn peak precipitation than the relatively less organized case. Numerical experiments with a weak large-scale forcing also attained a diurnal cycle similar to their counterparts with a strong forcing.

A diurnal convective cycle still occurred in the absence of the cloud-radiative forcing. Additionally, the cloud-radiative interaction had a negative influence on precipitation and convective activity and a positive impact on the anvil cloudiness, in contrast with general circulation modeling results. This finding and its physical interpretation warrant more comprehensive studies and probably impact the issue of prognostically modeled cloud and its radiative interaction.

There are two physically distinct processes potentially responsible for the simulated diurnal cycle. The first is related to the day–night differential radiative impact on the tropospheric static stability; the second is the horizontal gradient or inhomogeneity in the radiative heating and cooling profiles over the convective region and the surroundings. Sensitivity tests suggest that the first mechanism was the key player in regulating the diurnal variability, while the second was of secondary importance. This was probably because the simulated cloud clusters either moved fast or developed randomly in the domain; the location of the cloudy and surrounding regions were so variable with time that the differential heating could not persistently and cumulatively operate over a given area. We speculate that the cloud–cloud-free mechanism could be more important for quasi-stationary cloud clusters, a point worth further investigation. In other words, the radiative effect of clouds cannot be isolated from the issue of cloud system organization in a sheared atmosphere: this aspect has received scant attention in the large-scale modeling community.

Several other issues also deserve examination. For instance, how does the modeled diurnal cycle depend upon microphysics and radiation schemes? Preliminary sensitivity tests (not shown) indicate that the inclusion of ice phase was essential to realistically simulate the diurnal cycle. With warm rain microphysics alone, the simulation gave rise to a thick, domain-wide cloud sheet in the upper troposphere, which considerably reduced the insolation impact on the low- and midlevel atmospheric stratification and, consequently, the diurnal convective variability. Sensitivity tests should be conducted with a more sophisticated parameterization (i.e., a three-category ice-phase microphysics). Another issue is how the model results depend on the domain size. The current setup was to study mesoscale cloud clusters, and the simulated clear area is comparable to the cloudy area, as illustrated in Fig. 7. A much larger domain is required to study large cloud clusters. An adequate domain size is also necessary to produce a more typical ratio between the clear region and cloudy region, and this may affect the dominant operating mechanism in the diurnal cycle.

Acknowledgments. We thank Dr. W. W. Grabowski for his assistance in using the CCM2 radiation package in the cloud-resolving model. We are also appreciative of the thoughtful comments of Dr. W.-K. Tao and two anonymous reviewers.

REFERENCES

Albright, M. D., D. R. Mock, E. E. Recker, and R. J. Reed, 1981: A diagnostic study of the diurnal rainfall variation in the GATE B-scale area. *J. Atmos. Sci.,* **38,** 1429–1445.

——, E. E. Recker, and R. J. Reed, 1985: The diurnal variation of deep convection and inferred precipitation in the central tropical Pacific during January–February 1979. *Mon. Wea. Rev.,* **113,** 1663–1680.

Augustine, J. A., 1984: The diurnal variation of large-scale inferred rainfall over the tropical Pacific Ocean during August 1979. *Mon. Wea. Rev.,* **112,** 1745–1751.

Briegleb, B. P., 1992: Delta-Eddington approximation for solar radiation in the NCAR Community Climate Model. *J. Geophys. Res.,* **97,** 7603–7612.

Brier, G. W., and J. Simpson, 1969: Tropical cloudiness and rainfall related to pressure and tidal variations. *Quart. J. Roy. Meteor. Soc.,* **95,** 120–147.

Chang, A. T. C., L. S. Chiu, and G. Yang, 1995: Diurnal cycle of oceanic precipitation from SSM/I data. *Mon. Wea. Rev.,* **123,** 3371–3380.

Chen, S. S., and R. A. Houze Jr., 1997: Diurnal variation and life-cycle of deep convective systems over the tropical Pacific warm pool. *Quart. J. Roy. Meteor. Soc.,* **123,** 357–388.

Clark, T. L., W. D. Hall, and J. L. Coen, 1996: Source code documentation for the Clark-Hall cloud-scale model: Code version G3CH01. NCAR Tech. Note NCAR/TN-426+STR, 174 pp. [Available from National Center for Atmospheric Research, P. O. Box 3000, Boulder, CO 80307-3000.]

Deardorff, J. W., 1972: Parameterization of the planetary boundary layer for use in general circulation models. *Mon. Wea. Rev.,* **100,** 93–106.

Dudhia, J., 1989: Numerical study of convection observed during the Winter Monsoon Experiment using a mesoscale two-dimensional model. *J. Atmos. Sci.,* **46,** 3077–3107.

Ferrier, B. S., J. Simpson, and W.-K. Tao, 1996: Factors responsible for precipitation efficiencies in midlatitude and tropical squall simulations. *Mon. Wea. Rev.,* **124,** 2100–2125.

Fingerhut, W. A., 1978: A numerical model of a diurnally varying tropical cloud cluster disturbance. *Mon. Wea. Rev.,* **106,** 255–264.

Fu, Q., S. K. Krueger, and K. N. Liou, 1995: Interactions of radiation and convection in simulated tropical cloud clusters. *J. Atmos. Sci.,* **52,** 1310–1328.

Grabowski, W. W., X. Wu, and M. W. Moncrieff, 1996: Cloud-resolving modeling of tropical cloud systems during Phase III of GATE. Part I: Two-dimensional experiments. *J. Atmos. Sci.,* **53,** 3684–3709.

Gray, W. M., and R. W. Jacobson, 1977: Diurnal variation of deep cumulus convection. *Mon. Wea. Rev.,* **105,** 1171–1188.

Janowiak, J. E., P. A. Arkin, and M. Morrissey, 1994: An examination

of the diurnal cycle in oceanic tropical rainfall using satellite and in situ data. *Mon. Wea. Rev.,* **122,** 2296–2311.

Kessler, E., 1969: *On the Distribution of Water Substance in Atmospheric Circulations. Meteor. Monogr.,* No. 32, Amer. Meteor. Soc., 84 pp.

Kiehl, J. T., J. J. Hack, and B. P. Briegleb, 1994: The simulated earth radiation budget of the National Center for Atmospheric Research community climate model CCM2 and comparisons with the earth radiation. *J. Geophys. Res.,* **99,** 20 815–20 827.

Koenig, L. R., and F. W. Murray, 1976: Ice-bearing cumulus cloud evolution: Numerical simulation and general comparison against observations. *J. Appl. Meteor.,* **15,** 747–762.

Mapes, B. E., and R. A. Houze Jr., 1993: Cloud clusters and superclusters over the oceanic warm pool. *Mon. Wea. Wev.,* **121,** 1398–1415.

McBride, J. L., and W. M. Gray, 1980: Mass divergence in tropical weather systems. Paper I: Diurnal variation. *Quart. J. Roy. Meteor. Soc.,* **106,** 501–516.

McGarry, M. M., and R. J. Reed, 1978: Diurnal variations in convective activity and precipitation during phases II and III of GATE. *Mon. Wea. Rev.,* **106,** 101–113.

Meisner, B. N., and P. A. Arkin, 1987: Spatial and annual variations in the diurnal cycle of large-scale tropical convective cloudiness and precipitation. *Mon. Wea. Rev.,* **115,** 2009–2032.

Miller, R. A., and W. M. Frank, 1993: Radiative forcing of simulated tropical cloud clusters. *Mon. Wea. Rev.,* **121,** 482–498.

Moncrieff, M. W., 1981: A theory of organized steady convection and its transport properties. *Quart. J. Roy. Meteor. Soc.,* **107,** 29–50.

Murakami, M., 1983: Analysis of the deep convective activity over the Western Pacific and Southeast Asia. Part I: Diurnal variation. *J. Meteor. Soc. Japan,* **61,** 60–76.

Ramanathan, V., and P. Downey, 1986: A nonisothermal emissivity and absorptivity formulation for water vapor. *J. Geophys. Res.,* **91,** 8649–8666.

Randall, D. A., Harshvardhan, D. A. Dazlich, and T. G. Corsetti, 1989: Interactions among radiation, convection, and large-scale dynamics in a general circulation model. *J. Atmos. Sci.,* **46,** 1943–1970.

——, ——, and ——, 1991: Diurnal variability of the hydrologic cycle in a general circulation model. *J. Atmos. Sci.,* **48,** 40–62.

Reed, R. J., and K. D. Jaffe, 1981: Diurnal variation of summer convection over West Africa and the tropical Eastern Atlantic during 1974 and 1978. *Mon. Wea. Rev.,* **109,** 2527–2534.

Silva Dias, P. L., J. P. Bonatti, and V. E. Kousky, 1987: Diurnally forced tropical tropospheric circulation over South America. *Mon. Wea. Rev.,* **115,** 1465–1478.

Slingo, A., 1989: A GCM parameterization for the shortwave radiative properties of water clouds. *J. Atmos. Sci.,* **46,** 1419–1427.

Sui, C.-H., K.-M. Lau, Y. N. Takayabu, and D. A. Short, 1997: Diurnal variations in tropical oceanic cumulus convection during TOGA COARE. *J. Atmos. Sci.,* **54,** 639–655.

Tao, W.-K., and J. Simpson, 1984: Cloud interactions and merging: Numerical simulations. *J. Atmos. Sci.,* **41,** 2901–2917.

——, S. Lang, J. Simpson, C.-H. Sui, B. Ferrier, and M.-D. Chou, 1996: Mechanisms of cloud–radiation interaction in the Tropics and midlatitudes. *J. Atmos. Sci.,* **53,** 2624–2651.

Tripoli, G. J., and W. R. Cotton, 1989a: Numerical study of an observed orogenic mesoscale convective system. Part 1: Simulated genesis and comparison with observations. *Mon. Wea. Rev.,* **117,** 273–304.

——, and ——, 1989b: Numerical study of an observed orogenic mesoscale convective system. Part 2: Analysis of governing dynamics. *Mon. Wea. Rev.,* **117,** 305–328.

Wallace, J. M., 1975: Diurnal variations in precipitation and thunderstorm frequency over the conterminous United States. *Mon. Wea. Rev.,* **103,** 406–419.

Webster, P. J., and G. L. Stephens, 1980: Tropical upper-tropospheric extended clouds: Inferences from Winter MONEX. *J. Atmos. Sci.,* **37,** 1521–1541.

Wexler, R., 1983: Relative frequency and diurnal variation of high cold clouds in the tropical Atlantic and Pacific. *Mon. Wea. Rev.,* **111,** 1300–1304.

Xu, K.-M., and S. K. Krueger, 1991: Evaluation of cloudiness parameterization using a cumulus ensemble model. *Mon. Wea. Rev.,* **119,** 342–367.

——, and D. A. Randall, 1995: Impact of interactive radiative transfer on the macroscopic behavior of cumulus ensembles. Part II: Mechanisms for cloud–radiation interactions. *J. Atmos. Sci.,* **52,** 800–817.